Chemical Science

ROYAL SOCIETY OF CHEMISTRY

EDGE ARTICLE

View Article Online
View Journal | View Issue

Cite this: *Chem. Sci.*, 2025, **16**, 8282

All publication charges for this article have been paid for by the Royal Society of Chemistry

Received 20th March 2025
Accepted 4th April 2025

DOI: 10.1039/d5sc02149a

rsc.li/chemical-science

Manipulating room-temperature phosphorescence by electron–phonon coupling†

Liangwei Ma,‡ Muyu Cong,‡ Siyu Sun and Xiang Ma *

Designing and optimizing efficient organic room-temperature phosphorescent (RTP) materials remains a captivating yet challenging endeavour due to the inherent difficulties in generating and stabilizing triplet excitons. Here, we report a suite of highly efficient phosphors characterized by near-unity intersystem crossing (ISC) yields. Surprisingly, upon doping these dyes into a polyvinyl alcohol matrix, their phosphorescence quantum yields (Φ_P) spanned a wide range from 2.7% to 69.6%, governed by the position of the methyl substituent. Theoretical calculations and experimental results indicate that the variation in phosphorescence efficiency is primarily due to the strong electron–phonon coupling caused by the positional variation of the methyl substituents, rather than common factors such as ISC or energy levels. These findings provide a new insight into the design of high-performance organic RTP dyes.

In recent years, organic room-temperature phosphorescent (RTP) materials have garnered huge research interest due to their unique photophysical properties, such as long lifetimes and large Stokes shifts, which make them promising for applications in displays, bioimaging, anticounterfeiting, encryption, and electroluminescence.[1–9] However, the construction of highly efficient organic RTP materials remains a significant challenge. The difficulties in constructing these materials stem from three main reasons: (1) spin-forbidden intersystem crossing (ISC) process: ISC is a spin-forbidden process, making it difficult to efficiently generate triplet excited states through photoexcitation. (2) Slow radiative transition rates: the radiative transition rates of triplet states are relatively slow ($\sim 10^0$–10^6 s^{-1}), comparable to non-radiative relaxation processes caused by molecular vibration, rotation, or collision. This makes the triplet excited states highly susceptible to non-radiative deactivation. (3) Oxygen quenching: triplet excited states are easily quenched by oxygen through energy transfer processes.[6,10–19] To address these challenges and achieve highly efficient RTP materials, various strategies have been proposed: (1) designing specific molecular structures (*e.g.*, twisted molecular structures) or introducing heteroatoms, heavy atoms, or functional groups such as carbonyl groups into the molecular framework to enhance spin–orbit coupling (SOC) and promote ISC.[1,20–30] (2) Utilizing polymer matrices, crystallization, or macrocycles to create a rigid microenvironment for phosphors that restricts the molecular vibration, rotation, and collision, which result in non-radiative transitions, and isolates dyes from oxygen effectively.[29,31–40] Generally, molecular rotation and intermolecular collisions can be significantly suppressed or even eliminated in the solid state or in a rigid microenvironment.[41] However, molecular vibrations are much more difficult to effectively suppress. This can be evidenced by the fact that fine structures in luminescence spectra are often only observable at very low temperatures and enhancement of phosphorescence at lower temperatures.[10,15,40,42–44] Molecular vibrations are an intrinsic property related to electron–phonon coupling (EPC). Strong EPC typically implies strong molecular vibrational capability, which may lead to intense non-radiative transitions. Previous studies have already demonstrated that EPC is an important factor affecting the performance of organic optoelectronic materials.[45–47] However, in the research on RTP materials, which are more susceptible to non-radiative transitions, little attention was paid to this extremely important factor.[48] In current research, the general approach is to use a rigid microenvironment as an external means to suppress molecular vibrations. Theoretically, the ability of a rigid microenvironment is limited, with a specific threshold. When the intrinsic EPC is too strong, the molecular vibration can no longer be effectively suppressed, severely limiting the construction of highly efficient RTP dyes. Therefore, in the molecular design of phosphorescent dyes, EPC must be considered alongside SOC, electron configurations, and energy levels.

In this work, we systematically demonstrate the significant impact of EPC on the performance of phosphorescent dyes. As the position of the substituents changes, the ISC efficiency of these methyl-substituted thiochroman-4-one derivatives

Key Laboratory for Advanced Materials and Joint International Research Laboratory of Precision Chemistry and Molecular Engineering, Frontiers Science Center for Materiobiology and Dynamic Chemistry, School of Chemistry and Molecular Engineering, East China University of Science and Technology, Shanghai 200237, China. E-mail: maxiang@ecust.edu.cn

† Electronic supplementary information (ESI) available. See DOI: https://doi.org/10.1039/d5sc02149a

‡ These authors contributed equally to this work.

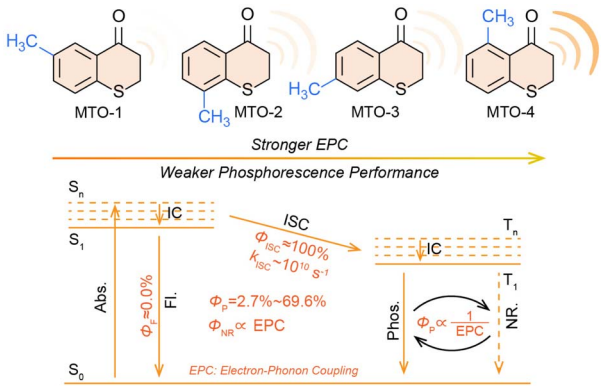

Scheme 1 Chemical structure of target compounds and the simplified Jablonski diagram for the transition process from the lowest excited state in aromatic compounds.

(MTOs, Scheme 1) approaches 100%, with the ISC rate constant (k_{ISC}) gradually increasing. In contrast, the phosphorescence quantum yield (Φ_P) decreases from 69.6% (MTO-1@PVA) to 2.7% (MTO-4@PVA) with the increase of k_{ISC}. Temperature-dependent emission spectra show that materials with lower Φ_P are more temperature-sensitive, indicating stronger EPC. Theoretical simulations reveal that MTO-4 has a Huang–Rhys factor of 23.06 at 82 cm^{-1}, while the Huang–Rhys factors of the other three compounds do not exceed 1.0, indicating that MTO-4 has significantly stronger EPC. Combined with the temperature-dependent experiments, it is determined that the significant decrease in phosphorescence efficiency is primarily due to the excessively strong EPC in MTO-4, which causes molecular vibrations to exceed the threshold that the polyvinyl alcohol (PVA) matrix can effectively suppress. This work highlights the critical role of EPC in the design of efficient RTP materials and provides new insights into the mechanisms governing phosphorescence performance.

The comprehensive synthetic protocols for MTO compounds are elaborately outlined in the ESI.† Their chemical structures were meticulously authenticated through ^{1}H NMR, ^{13}C NMR, and HRMS analyses. Upon dissolution in dichloromethane (DCM), the four dyes displayed strikingly analogous absorption spectra (Fig. 1a), with their maximum absorption peaks consistently centred around 350 nm. The subtle shifts in the maximum emission wavelengths can be attributed to the subtle perturbations induced by the varying methyl substituent positions on the energy levels of the frontier orbitals. This observation is consistent with the fact that the methyl group lacks π-orbitals to conjugate with the frontier orbitals of thiochroman-4-one. However, a marked disparity was observed in the fluorescence intensities among the dyes as the methyl substituent position varied (Fig. 1a). The fluorescence quantum yield (Φ_F) was found to be 1.19% in DCM when the methyl group occupied the 6-substituent position (Table S1†), whereas it was virtually quenched (Φ_F = 0.25%) when situated at the 5-substituent position. Furthermore, substantial differences in the fluorescence lifetimes of these compounds were discernible (Fig. 1b and S1†), indicative of substantial variations in the relaxation dynamics of the lowest singlet excited state (S_1).

To unravel the unusual impact of the methyl group on the photophysical properties, density functional theory (DFT) and time-dependent DFT (TDDFT) calculations were conducted using the G09 program with the M062x/aug-cc-pVTZ level of theory.[39,49] As depicted in Table S2,† the $S_0 \rightarrow S_1$ transition for these compounds predominantly involved HOMO/HOMO-2 → LUMO transitions. Despite their similar molecular frameworks (Fig. S2†), the contribution from the HOMO → LUMO transition, which characterizes a π → π* transition, progressively dwindled from 20.1% to 0% as the methyl substituent position varied. Notably, the HOMO-2 → LUMO transition, constituting the dominant contribution to the $S_0 \rightarrow S_1$ transition, represents a typical n → π* transition. Thus, the $S_0 \rightarrow S_1$ transition for these compounds is classified as a forbidden transition due to the non-conservation of orbital angular momentum. Correspondingly, with the decline in the HOMO → LUMO transition contribution, the *f* of these compounds plummeted from 0.0165 to 0.0002 (Table S2†). Conversely, the $S_0 \rightarrow S_2$ transition for these compounds was primarily driven by the HOMO → LUMO transition, representing a spin-allowed process. Consequently, the $S_0 \rightarrow S_1$ transition is designated as a dark state.[50] Hence, the maximum absorption peak for these compounds is attributed to the $S_0 \rightarrow S_2$ transition. The shoulder peak observed at 370 nm in the absorption spectrum of MTO-1 is assigned to the $S_0 \rightarrow S_1$ transition due to its weak yet non-negligible *f* value.

The $S_1 \rightarrow S_0$ transition mirrored the trends observed for the $S_0 \rightarrow S_1$ transition (Table S2†). For MTO-1, the $S_1 \rightarrow S_0$ transition was primarily governed by the HOMO → LUMO transition (95.4%), with a minor contribution from the HOMO-2 → LUMO transition (2.2%). However, the contribution from the HOMO → LUMO transition significantly declined to 24.1% for MTO-2, further dwindling to 18.5% and 8.6% for MTO-3 and MTO-4, respectively. Concurrently, the HOMO-2 → LUMO transition contribution escalated to 62.3%, 67.6%, and 76.9% for MTO-2, MTO-3, and MTO-4. As a result, the fluorescence transition for these compounds transformed into a forbidden process as the methyl substituent position varied. Comparable phenomena were also evident in different solvents. The consistent maximum absorption and emission wavelengths of MTO-1 across various aprotic solvents with differing polarities supported the π → π* nature of the transition (Fig. 1c). An anomalous redshift in both absorption and emission spectra was observed for these compounds in protic solvents, accompanied by a marked increase in emission intensity (Fig. 1d). Correspondingly, the Φ_F increased to 6.67% in methanol. This abnormal enhancement and redshift were attributed to hydrogen bonding interactions between the solvent and the carbonyl group of MTOs.[51]

Previous studies have established thiochroman-4-one derivatives as promising phosphorescent dyes with high ISC efficiency.[18,52,53] Hence, the photophysical properties of these dyes were further investigated in 2-methyltetrahydrofuran at 77 K. As depicted in Fig. 1e, a broad emission band spanning 420–620 nm, adorned with a fine structure, was discernible in the steady-state spectra. Remarkably, the phosphorescence spectra of these compounds closely resembled their corresponding steady-state emission spectra. Most intriguingly, no appreciable

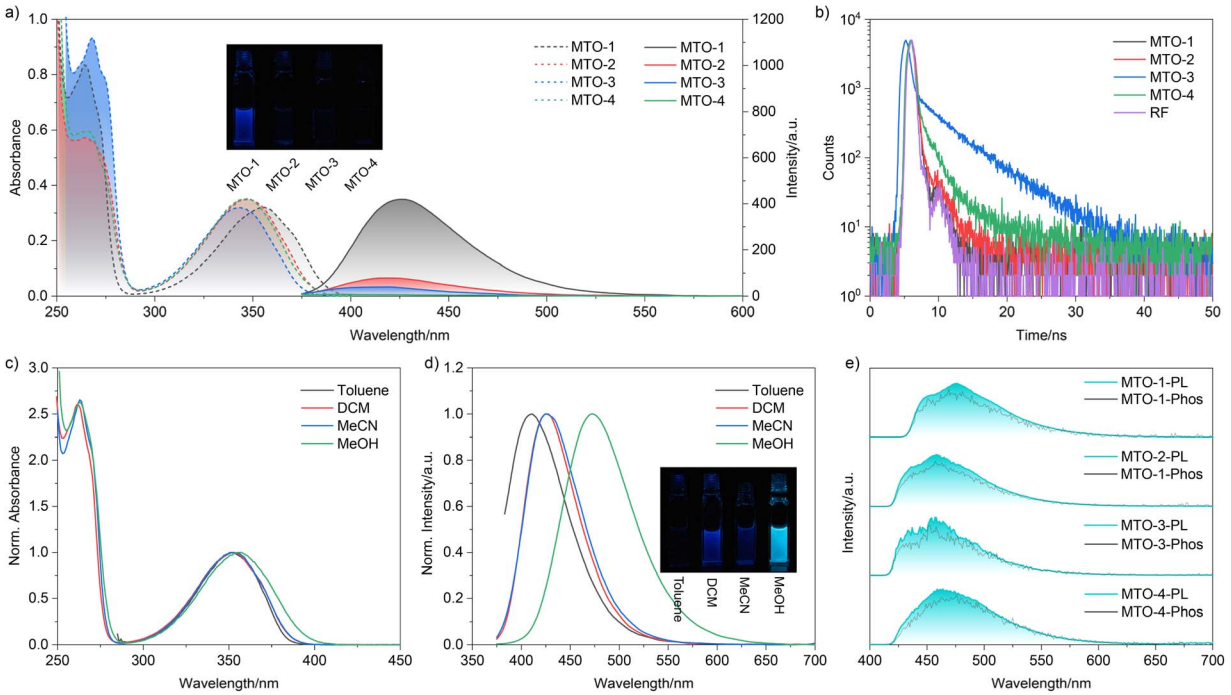

Fig. 1 a) Absorption and emission spectra of MTOs in DCM; (b) lifetime spectra of MTOs in DCM; absorption (c) and emission (d) spectra of MTO-1 in different solvents; (e) steady-state and phosphorescence spectra of MTOs in MTHF at 77 K.

fluorescence emission was detected at 77 K, strongly suggesting an efficient ISC process for these compounds.

Subsequently, these compounds were embedded in a PVA matrix, known to effectively suppress non-radiative transitions and isolate oxygen,[15,54] thus enabling the fabrication of RTP materials. Powder X-ray diffraction analysis of these films (Fig. S3†) revealed an absence of discernible diffraction peaks, signifying their amorphous nature. Analogous to the behaviour of the dyes in solution, the maximum absorption peaks for these films were found around 350 nm (Fig. 2a). The steady-state emission spectra of the films displayed structureless emission bands spanning 380–700 nm (Fig. 2b). Specifically, MTO-1@PVA showcased a maximum emission wavelength at 485 nm, accompanied by a shoulder peak at approximately 420 nm. Notably, the shoulder peak vanished in the phosphorescence emission spectrum, implying that it corresponded to the weak fluorescence emission of MTO-1@PVA, while the dominant emission peak at 485 nm was attributed to the phosphorescence emission. This attribution was further substantiated by lifetime measurements performed at different temperatures (Fig. S4†). The phosphorescence lifetime of MTO-1@PVA was measured to be 21.92 ms at 297 K (Fig. 2c). Its photoluminescence quantum yield (Φ_{PL}) was calculated to be 69.6% (Fig. S5† and Table 1). The excellent agreement between the excitation and absorption spectra (Fig. 2a) confirmed the origin of phosphorescence from MTO-1. Similarly, MTO-2@PVA displayed a much weaker shoulder peak around 420 nm. In contrast, MTO-3@PVA displayed a structureless emission peak at 460 nm, which was confidently assigned to the phosphorescence emission. The Φ_{PL} values for MTO-2@PVA and MTO-3@PVA were determined to be 47.7% and 48.8%, respectively. Thus, it can be concluded that MTO-1@PVA, MTO-2@PVA, and MTO-3@PVA are essentially pure phosphorescent materials, a rarity among metal-free substances. However, MTO-4@PVA exhibited a distinct behaviour. As evident in Fig. 2b, the maximum emission wavelength of MTO-4@PVA was positioned at 435 nm in the steady-state emission spectrum, while its phosphorescence emission wavelength was identified as 470 nm, implying that the phosphorescence emission of MTO-4 was significantly weaker than its fluorescence emission within the PVA matrix. Correspondingly, the Φ_{PL} of MTO-4@PVA was measured to be a mere 2.7%. The phosphorescence lifetime for MTO-4@PVA was found to be 12.0 ms. The fluorescence lifetimes of all films under scrutiny ranged from 1.44 to 2.47 ns (Fig. 2d). It is particularly noteworthy that MTO-1@PVA and MTO-4@PVA exhibited comparable decay patterns and lifetimes (2.34 and 2.47 ns, respectively). Meanwhile, the lifetime spectra and parameters of MTO-2@PVA closely resembled those of MTO-3@PVA.

To delve deeper into the influence of the methyl group substituent position on the ISC process, TDDFT and ORCA calculations were also performed.[18,23] As previously discussed, the $S_1 \rightarrow S_0$ transition in MTOs progressively transitioned from a $\pi \rightarrow \pi^*$ to an $n \rightarrow \pi^*$ character with the change in the methyl group position. However, no conspicuous alteration in the frontier orbital distribution was observed (Fig. S2 and Table S2†). The energy levels of T_1 and T_2 exhibited slight fluctuations with the varying substituent positions (Table S2†). Notably, T_2 represented the highest triplet state, often being either close to or lower in energy than the S_1 state. Hence, $S_1 \rightarrow T_1$ and $S_1 \rightarrow T_2$

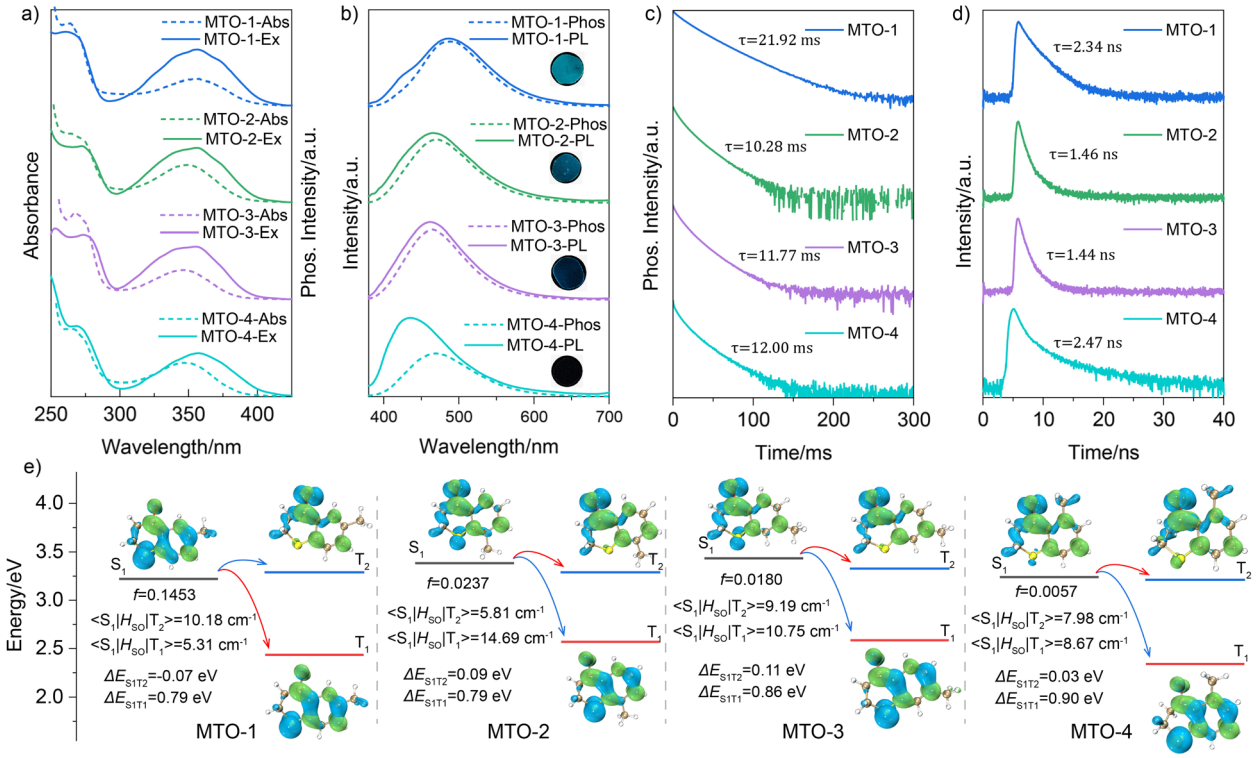

Fig. 2 (a) Absorption and phosphorescence excitation spectra of MTOs in the PVA matrix; (b) steady-state (solid line) and phosphorescence spectra (dashed line) of MTOs in the PVA matrix; phosphorescence (c) and fluorescence (d) lifetime spectra of MTOs in the PVA matrix; (e) electron–hole distribution and energy levels of different excited states.

transitions were identified as plausible ISC pathways for generating triplet excitons. Fig. 2e reveals that the hole in the S_0 → T_1 transition of MTOs is primarily localized on the sulfur atom and benzene rings, corresponding to π orbitals, while the electron is primarily distributed over the benzene and carbonyl moieties, associated with π* orbitals. Although the electron distribution in the S_0 → T_2 transition mirrors that of the S_0 → T_1 transition, the hole is primarily contributed by the n orbital of the carbonyl moiety. Consequently, the S_1 → T_1 ISC process evolved from a forbidden to an allowed transition as the substituent position changed, according to El-Sayed's rule. Conversely, the S_1 → T_2 ISC process transformed from an allowed to a forbidden transition with the variation in the substituent position. ORCA calculations further substantiated the significant impact of the methyl substituent position on the SOC, which is intricately linked to the ISC process.

Femtosecond TA spectra of MTOs in the PVA matrix were recorded and are presented in Fig. 3 and S6.† No ground state bleach (GSB) signal was observable due to their absorptions lying outside our detection wavelength range, nor was any stimulated emission (SE) signal detected. A distinct excited state absorption (ESA) signal was promptly detected for MTO-1@PVA post-excitation (Fig. 3a). The initially formed ESA band featured a peak around 620 nm with a shoulder at approximately 525 nm (Fig. 3b). Within the first 200 ps, it evolved into a long-lived ESA band with peaks at 470 nm and 610 nm. Analogous TA spectra were also evident for MTO-2@PVA and MTO-3@PVA (Fig. S6a and b†). Remarkably, MTO-4@PVA displayed a markedly different TA spectrum

Table 1 Photophysical parameters of MTOs in the PVA matrix

	λ_{Abs}/nm	λ_F/nm	λ_P/nm	τ_F/ns	τ_P/ms	Φ_{PL}/%	[a] Φ_{ISC}/%	[b] k_{ISC}/s^{-1}	[c] k_P/s^{-1}	[d] k_{nr}/s^{-1}
MTO-1@PVA	356	423	488	2.34	21.92	69.6	99.999	1.50×10^{10}	31.75	13.87
MTO-2@PVA	349	n.d.	470	1.46	10.28	47.7	99.995	1.75×10^{10}	46.40	50.88
MTO-3@PVA	345	n.d.	464	1.44	11.77	48.8	99.996	2.05×10^{10}	41.46	43.50
MTO-4@PVA	347	n.d.	468	2.47	12.00	2.7	99.995	2.55×10^{10}	2.25	81.08

[a] $\Phi_{ISC} = \frac{k_T}{k_S}$, where k_S is the deactivation rate of the singlet excited state, and k_T is the generation rate of the triplet excited state. k_S and k_T are determined according to the global fitting results of TA spectra. [b] $k_{ISC} = \frac{1}{k_T}$. [c] $k_P = \frac{\Phi_P}{\Phi_{ISC}\tau_P}$. [d] $k_{nr} = \frac{1-\Phi_P}{\Phi_{ISC}\tau_P}$; n.d. – too weak to record.

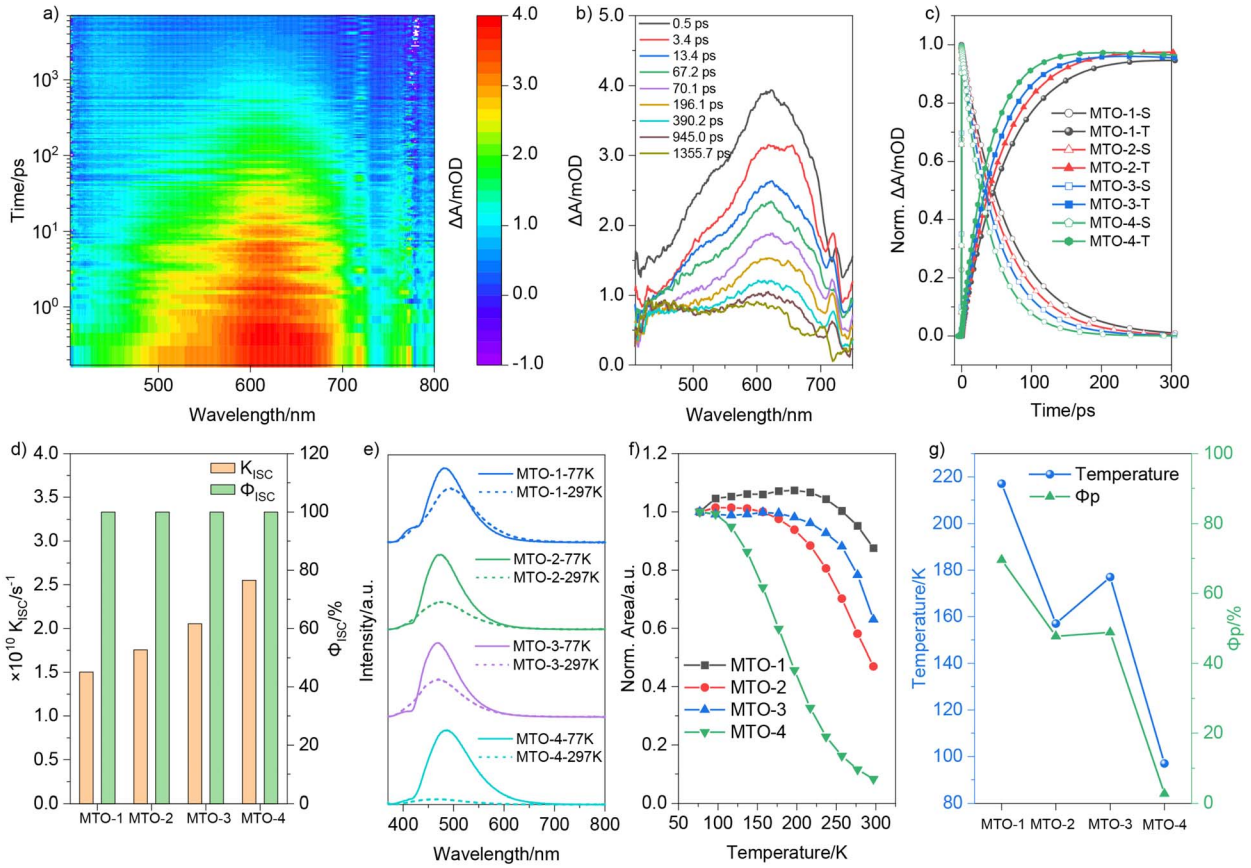

Fig. 3 (a) Femtosecond broadband TA spectra of MTO-1 in PVA under 320 nm excitation; (b) TA spectra of MTO-1 at different pump-probe delay times; (c) normalized singlet and triplet state kinetics curves of MTOs in the PVA matrix; (d) the calculated Φ_{ISC} and k_{ISC} of MTOs according to DADS data; (e) steady-state spectra of MTOs in the PVA matrix at 77 K and 297 K; (f) normalized emission spectra area of MTOs in the PVA matrix at different temperatures; (g) transition temperature points and Φ_P of MTOs in the PVA matrix.

compared to the other three films (Fig. S6c†). A distinct ESA signal spanning 400–600 nm, with peaks at 405 nm and 485 nm, was observed. The initial ESA band transformed into a long-lived ESA band spanning 400–600 nm, centred at 450 nm, within the first 100 ps (Fig. S6f†). Decay-associated difference spectra (DADS) for MTO-1@PVA were extracted *via* global analysis of the femtosecond TA data (Fig. S7†). The first decay-associated difference spectrum was attributed to the absorption of the singlet state (Fig. S7,† black line), displaying a broad signal in the 410–700 nm range with peaks around 520 nm and 620 nm, consistent with species present in the first 300 ps. The subsequent DADS was assigned to the absorption of the triplet state (Fig. S7,† red line), given its slow generation and decay within the 7 ns detection window. This spectrum exhibited a broad signal in the 410–700 nm range, with peaks around 450 nm and 615 nm. Comparable DADS were also discernible for the remaining three films (Fig. S6†). The decay kinetics curves of the singlet excited state and the generation kinetics of the triplet state of MTOs in the PVA matrix are compiled in Fig. 3c. Notably, the decay rate of the singlet excited state showed a pronounced increase from MTO-1 to MTO-4. The near-symmetric kinetics curves of decay and generation implied a highly efficient ISC process. The ISC yields (Φ_{ISC}) of MTOs were estimated to be >99.9% based on the kinetic parameters (Fig. 3d).[55] The k_{ISC} for MTO-1 was calculated to be 1.50 × 1010 s^{-1}, increasing to 1.75 × 1010 s^{-1} and 2.05 × 1010 s^{-1} for MTO-2 and MTO-3, respectively. MTO-4 displayed the highest k_{ISC}, reaching up to 2.55 × 10^{10} s^{-1}. However, the Φ_P of MTOs in the PVA matrix decreased from 69.6% to 2.7% as k_{ISC} increased. The TA data indicate that the ISC in the MTO series of compounds is highly efficient. Therefore, the phosphorescence quenching observed in MTO-4@PVA is unlikely to be due to issues with the generation of triplet excitons. Instead, strong non-radiative transitions are likely the primary cause.

To exclude the possibility of oxygen-induced non-radiative transitions in the PVA matrix, the emission spectra of MTO-4@PVA were initially measured under different atmospheres. As depicted in Fig. S8,† no noticeable change in phosphorescence intensity was observed when the film atmosphere was switched from air to argon. The phosphorescence intensity of MTO-4@PVA significantly intensified in the steady-state spectrum upon decreasing the temperature from 297 K to 77 K (Fig. 3e). Specifically, the area of the emission peak grew by a factor of 12.1 with decreasing temperature. In comparison, MTO-1@PVA, MTO-2@PVA, and MTO-3@PVA exhibited increases of 1.1, 2.1, and 1.6 times, respectively. A pronounced

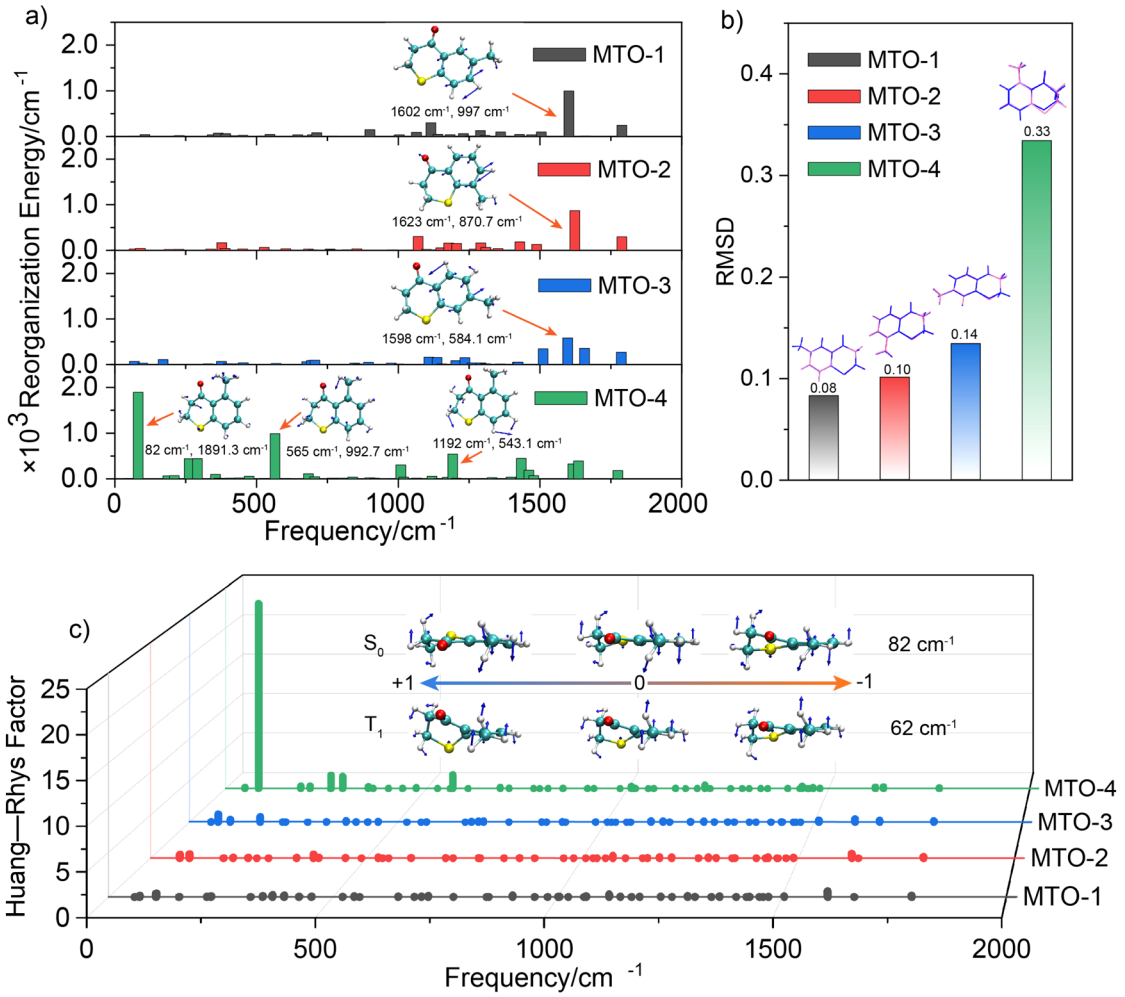

Fig. 4 (a) Calculated reorganization energies of the $T_1 \rightarrow S_0$ transition are plotted against the frequencies of MTOs. Representative high-intensity (>500 cm^{-1}) vibration modes are shown as insets; (b) schematic distribution of RMSD $T_0 \rightarrow S_0$ values; (c) Huang–Rhys factors of MTOs from T_1 to S_0. The insets show the most representative intramolecular vibration modes of MTO-4 in S_0 and T_1 states.

elongation in the phosphorescence lifetime was also observed as the temperature dropped from 297 K to 77 K. The emission spectrum areas of MTOs in the PVA matrix at various temperatures were meticulously analysed (Fig. S9†) and plotted in Fig. 3f. The area of MTO-1@PVA showed a marginal increase when the temperature increased from 77 K to 97 K. A distinct decline, signifying the onset of triplet exciton quenching by molecular thermal motion, ensued once the temperature exceeded 217 K. Similar trends were observed for the remaining three films. The areas of MTO-2@PVA, MTO-3@PVA, and MTO-4@PVA started to diminish when the temperature surpassed 157 K, 177 K, and 97 K, respectively. Notably, MTO-4@PVA displayed a much steeper decrease rate compared to the other three films. Intriguingly, the transition temperature points followed the same trend as Φ_P (Fig. 3g). The lower transition temperature points implied that triplet excitons in these films were more susceptible to quenching by molecular thermal vibration, hinting at a large k_{nr}.

To further understand the non-radiative pathways and the underlying mechanisms responsible for the phosphorescence quenching, we further used the DFT calculations to quantitatively assess the vibrational freedom of these compounds at the B3LYP/def2SVP level. The reorganization energy *versus* different normal vibrational modes is computed to evaluate the feasibility of a phosphor in its T_1 state to decay *via* nonradiative decay (Fig. 4a). Compared to MTO-1, MTO-2 shows a slight increase in vibration at a low-frequency mode (377 cm^{-1}), whereas MTO-3 primarily exhibits a slight increase in high-frequency vibration modes. The subtle changes in the vibrational modes of MTO-2 and MTO-3 may explain the decrease in their Φ_P. MTO-4 has a remarkably high reorganization energy of 1891.3 cm^{-1} at a vibrational mode of 82 cm^{-1}. Additionally, the reorganization energies at 565 cm^{-1} and 1192 cm^{-1} are both greater than 500 cm^{-1}. The significant increase in vibrational modes may explain the strong non-radiative transitions in MTO-4. Further analysis of the root mean square deviation (RMSD) of this series of compounds revealed that, with the change in the position of the substituents, the difference between the optimal configurations of the T_1 state and the S_0 state gradually increases (Fig. 4b). Specifically, MTO-1 has the

smallest RMSD value of 0.08, whereas MTO-4 has the largest, at 0.33—an increase of about four times. The large RMSD value of MTO-4 indicates stronger molecular vibrational behavior, providing more opportunities for non-radiative relaxation. We further calculated the Huang–Rhys factors of this series of compounds to characterize their EPC. As shown in Fig. 4c, the Huang–Rhys factors of MTO-1, MTO-2, and MTO-3 for various vibrational modes do not exceed 1. However, MTO-4 has four vibrational modes with Huang–Rhys factors exceeding 1.0, including a staggering 23.06 at 82 cm^{-1}. Such a high Huang–Rhys factor indicates strong EPC in MTO-4. Therefore, despite having similar electronic structures and energy levels in the S_0 and T_1 states compared to the other three compounds, the T_1 state of MTO-4 is highly susceptible to non-radiative deactivation.

Conclusions

In summary, a suite of efficient RTP materials was engineered by elaborate molecular designing. The $S_1 \rightarrow S_0$ transition characteristics was effectively modulated between $\pi \rightarrow \pi^*$ and $n \rightarrow \pi^*$ transitions by altering the methyl group substituent position. All synthesized dyes displayed near-unity Φ_{ISC} values. The k_{ISC} increased gradually from MTO-1 to MTO-4 as the methyl group substituent position varied. However, contrary to expectations, the Φ_P decreased from 69.6% to 2.7% alongside the rise in k_{ISC}. Theoretical calculations and experimental results indicate that the quenching of phosphorescence is primarily due to the strong EPC caused by the positional variation of the methyl substituents. This finding contrasts with common factors such as ISC or changes in energy levels, which are often considered in the context of phosphorescence quenching. The positional changes of the methyl groups significantly influence the vibrational modes and the interaction between electronic and vibrational states, leading to enhanced non-radiative relaxation and, consequently, the observed quenching of phosphorescence. These findings provide a new insight into the design of high-performance RTP dyes.

Data availability

All the data are available in the ESI.†

Author contributions

L. Ma, S. Sun, and X. Ma designed the materials and conceived the project. L. Ma conducted the molecule synthesis and characterization. M. Cong performed TA experiments. L. Ma and X. Ma wrote the manuscript. All authors engaged in discussions and conducted data analysis.

Conflicts of interest

There are no conflicts to declare.

Acknowledgements

We gratefully acknowledge the financial support from the National Natural Science Foundation of China (22125803, T2488302, 22020102006 and 22305080), Science and Technology Commission of Shanghai Municipality (Grant No. 24DX1400200), and the Fundamental Research Funds for the Central Universities.

References

1 Z. Wang, X. Cheng, Y. Xie, S. Liu, M. Dong, J. Zhao, F. Liang, Z. An and W. Huang, Recent Advances in Organic Room-Temperature Phosphorescence of Heteroatom (B/S/P)-Containing Chromophores, *CCS Chem.*, 2023, **5**, 292–309.
2 K. Jinnai, R. Kabe, Z. Lin and C. Adachi, Organic long-persistent luminescence stimulated by visible light in p-type systems based on organic photoredox catalyst dopants, *Nat. Mater.*, 2022, **21**, 338–344.
3 B. Ding, X. Ma and H. Tian, Recent Advances of Pure Organic Room Temperature Phosphorescence Based on Functional Polymers, *Acc. Mater. Res.*, 2023, **4**, 827–838.
4 L. Xu, H. Wei, G. Xie, B. Xu and J. Zhao, Ultralong MRTADF and Room-Temperature Phosphorescence Enabled Color-Tunable and High-Temperature Dual-Mode Organic Afterglow from Indolo[3,2-b]carbazole, *Adv. Funct. Mater.*, 2024, **34**, 2402428.
5 Y. Zhao, J. Yang, C. Liang, Z. Wang, Y. Zhang, G. Li, J. Qu, X. Wang, Y. Zhang, P. Sun, J. Shi, B. Tong, H. Y. Xie, Z. Cai and Y. Dong, Fused-Ring Pyrrole-Based Near-Infrared Emissive Organic RTP Material for Persistent Afterglow Bioimaging, *Angew. Chem., Int. Ed.*, 2023, **63**, e202317431.
6 J. Yu, Z. Sun, H. Ma, C. Wang, W. Huang, Z. He, W. Wu, H. Hu, W. Zhao and W.-H. Zhu, Efficient Visible-Light-Activated Ultra-Long Room-Temperature Phosphorescence Triggered by Multi-Esterification, *Angew. Chem., Int. Ed.*, 2023, **135**, e202316647.
7 Z. Xu, Z. Wang, W. Yao, Y. Gao, Y. Li, H. Shi, W. Huang and Z. An, Supercooled Liquids with Dynamic Room Temperature Phosphorescence Using Terminal Hydroxyl Engineering, *Angew. Chem., Int. Ed.*, 2023, **62**, e202301564.
8 Y. Li, Z. Huang, A. Shao, Z. Wu, Z. He, H. Tian and X. Ma, Aqueous up-conversion organic phosphorescence and tunable dual emission in a single-molecular emitter, *Chem. Sci.*, 2025, DOI: **10.1039/d4sc08330j**.
9 H. Sun, Y. Xiao, Y. He, X. Wei, J. Zou, Y. Luo, Y. Wu, J. Zhao, V. K.-M. Au and T. Yu, 3D printable organic room-temperature phosphorescent materials and printed real-time sensing and display devices, *Chem. Sci.*, 2025, **16**, 5299–5309.
10 T. Wang, A. K. Gupta, S. Wu, A. M. Z. Slawin and E. Zysman-Colman, Conjugation-Modulated Excitonic Coupling Brightens Multiple Triplet Excited States, *J. Am. Chem. Soc.*, 2023, **145**, 1945–1954.
11 Q. Peng, H. Ma and Z. Shuai, Theory of Long-Lived Room-Temperature Phosphorescence in Organic Aggregates, *Acc. Chem. Res.*, 2021, **54**, 940–949.

12 Q. Meng, S. Gan, Q. Cheng, Z. Jiang, H. Zhu, G. Xie, R. Liu, S. Zhu and H. Zhu, Efficient tuning of nitrogen-doped carbon dots phosphorescence based on substrate regulation for multicolor and time-dependent anti-counterfeiting, *Dyes Pigm.*, 2024, **224**, 112002.
13 X. Ma, J. Wang and H. Tian, Assembling-Induced Emission: An Efficient Approach for Amorphous Metal-Free Organic Emitting Materials with Room-Temperature Phosphorescence, *Acc. Chem. Res.*, 2019, **52**, 738–748.
14 L. Ma and X. Ma, Recent advances in room-temperature phosphorescent materials by manipulating intermolecular interactions, *Sci. China Chem.*, 2022, **66**, 304–314.
15 L. Gao, J. Huang, L. Qu, X. Chen, Y. Zhu, C. Li, Q. Tian, Y. Zhao and C. Yang, Stepwise taming of triplet excitons *via* multiple confinements in intrinsic polymers for long-lived room-temperature phosphorescence, *Nat. Commun.*, 2023, **14**, 7252.
16 L. Wei, F. Gao, C. He, Q. He, P. Jin, Y. Rong, T. Zhao, C. Yang and W. Wu, A new sensitization strategy for achieving organic RTP in aqueous solution: tunable RTP and UC emission in supramolecular TTA-UC systems, *Sci. China Chem.*, 2023, **66**, 3546–3554.
17 T. Wang, M. Liu, J. Mao, Y. Liang, L. Wang, D. Liu, T. Wang and W. Hu, Recent advances in long-persistent luminescence materials based on host–guest architecture, *Chinese Chem. Lett.*, 2024, **35**, 108385.
18 L. Ma, S. Sun, B. Ding, X. Ma and H. Tian, Highly Efficient Room-Temperature Phosphorescence Based on Single-Benzene Structure Molecules and Photoactivated Luminescence with Afterglow, *Adv. Funct. Mater.*, 2021, **31**, 2010659.
19 L. Ma, Y. Liu, X. Jin, T. Jiang, L. Zhou, Q. Wang, H. Tian and X. Ma, Triplet Exciplex Mediated Multi-Color Ultra-Long Afterglow Materials, *Angew. Chem., Int. Ed.*, 2025, **64**, e202500847.
20 M. A. El-Sayed, Spin-Orbit Coupling and the Radiationless Processes in Nitrogen Heterocyclics, *J. Chem. Phys.*, 1963, **38**, 2834–2838.
21 J. Yang, M. Fang and Z. Li, Stimulus-Responsive Room Temperature Phosphorescence Materials: Internal Mechanism, Design Strategy, and Potential Application, *Acc. Mater. Res.*, 2021, **2**, 644–654.
22 Z. Chen, X. Chen, D. Ma, Z. Mao, J. Zhao and Z. Chi, Synergetic Conformational Regulations in Ground and Excited States for Realizing Stimulus-Responsive and Wide-Tuning Room-Temperature Phosphorescence, *J. Am. Chem. Soc.*, 2023, **145**, 16748–16759.
23 H. Ma, Q. Peng, Z. An, W. Huang and Z. Shuai, Efficient and Long-lived Room Temperature Organic Phosphorescence: Theoretical Descriptors for Molecular Designs, *J. Am. Chem. Soc.*, 2018, **141**, 1010–1015.
24 M. Gao, Y. Tian, X. Li, Y. Gong, M. Fang, J. Yang and Z. Li, The Effect of Molecular Conformations and Simulated "Self-Doping" in Phenothiazine Derivatives on Room-Temperature Phosphorescence, *Angew. Chem., Int. Ed.*, 2023, **62**, e202214908.
25 T. Zhang, X. Ma, H. Wu, L. Zhu, Y. Zhao and H. Tian, Molecular Engineering for Metal-Free Amorphous Materials with Room-Temperature Phosphorescence, *Angew. Chem., Int. Ed.*, 2020, **59**, 11206–11216.
26 N. J. Turro, V. Ramamurthy and J. C. Scaiano, *Modern Molecular Photochemistry of Organic Molecules*, University Science Books, 2009, ISBN: 978-1-891389-25-2.
27 C. A. M. Salla, G. Farias, M. Rouzieres, P. Dechambenoit, F. Durola, H. R. Bock, B. de Souza and I. H. Bechtold, Persistent solid-state phosphorescence and delayed fluorescence at room temperature from a twisted hydrocarbon, *Angew. Chem., Int. Ed.*, 2019, **58**, 6982–6986.
28 Z. Yuan, J. Wang, L. Chen, L. Zou, X. Gong and X. Ma, Methanol Dynamically Activated Room-Temperature Phosphorescence from a Twisted 4-Bromobiphenyl System, *CCS Chem.*, 2020, **2**, 158–167.
29 S. Kuila, K. V. Rao, S. Garain, P. K. Samanta, S. Das, S. K. Pati, M. Eswaramoorthy and S. J. George, Aqueous Phase Phosphorescence: Ambient Triplet Harvesting of Purely Organic Phosphors *via* Supramolecular Scaffolding, *Angew. Chem., Int. Ed.*, 2018, **57**, 17115–17119.
30 Z. Xie, Z. Mao, H. Wang, Y. Xiao, X. Zhang, T. Yu, Z. An and W. Huang, Dual-channel mechano-phosphorescence: a combined locking effect with twisted molecular structures and robust interactions, *Light Sci. Appl.*, 2024, **13**, 85.
31 X. Ma, C. Xu, J. Wang and H. Tian, Amorphous Pure Organic Polymers for Heavy-Atom-Free Efficient Room-Temperature Phosphorescence Emission, *Angew. Chem., Int. Ed.*, 2018, **57**, 10854–10858.
32 Z. A. Yan, X. Lin, S. Sun, X. Ma and H. Tian, Activating Room-Temperature Phosphorescence of Organic Luminophores *via* External Heavy-Atom Effect and Rigidity of Ionic Polymer Matrix, *Angew. Chem., Int. Ed.*, 2021, **60**, 19735–19739.
33 Z. Yang, C. Xu, W. Li, Z. Mao, X. Ge, Q. Huang, H. Deng, J. Zhao, F. L. Gu, Y. Zhang and Z. Chi, Boosting the Quantum Efficiency of Ultralong Organic Phosphorescence up to 52% *via* Intramolecular Halogen Bonding, *Angew. Chem., Int. Ed.*, 2020, **59**, 17451–17455.
34 E. Hamzehpoor, C. Ruchlin, Y. Tao, C. H. Liu, H. M. Titi and D. F. Perepichka, Efficient room-temperature phosphorescence of covalent organic frameworks through covalent halogen doping, *Nat. Chem.*, 2023, **15**, 83–90.
35 C. Li, X. Li and Q. Wang, Supramolecular self-assembling strategy for constructing cucurbit[6]uril derivative-based amorphous pure organic room-temperature phosphorescence complex featuring extra-high efficiency, *Chinese Chem. Lett.*, 2022, **33**, 877–880.
36 J. Wang, Z. Huang, X. Ma and H. Tian, Visible-Light-Excited Room-Temperature Phosphorescence in Water by Cucurbit[8]uril-Mediated Supramolecular Assembly, *Angew. Chem., Int. Ed.*, 2020, **59**, 9928–9933.
37 X. K. Ma, W. Zhang, Z. Liu, H. Zhang, B. Zhang and Y. Liu, Supramolecular Pins with Ultralong Efficient Phosphorescence, *Adv. Mater.*, 2021, **33**, 2007476.

38 W. Ye, H. Ma, H. Shi, H. Wang, A. Lv, L. Bian, M. Zhang, C. Ma, K. Ling, M. Gu, Y. Mao, X. Yao, C. Gao, K. Shen, W. Jia, J. Zhi, S. Cai, Z. Song, J. Li, Y. Zhang, S. Lu, K. Liu, C. Dong, Q. Wang, Y. Zhou, W. Yao, Y. Zhang, H. Zhang, Z. Zhang, X. Hang, Z. An, X. Liu and W. Huang, Confining isolated chromophores for highly efficient blue phosphorescence, *Nat. Mater.*, 2021, **20**, 1539–1544.

39 H. Wang, H. Ma, N. Gan, K. Qin, Z. Song, A. Lv, K. Wang, W. Ye, X. Yao, C. Zhou, X. Wang, Z. Zhou, S. Yang, L. Yang, C. Bo, H. Shi, F. Huo, G. Li, W. Huang and Z. An, Abnormal thermally-stimulated dynamic organic phosphorescence, *Nat. Commun.*, 2024, **15**, 2134.

40 G. Wang, X. Chen, Y. Zeng, X. Li, X. Wang and K. Zhang, Dual-Mechanism Design Strategy for High-Efficiency and Long-Lived Organic Afterglow Materials, *J. Am. Chem. Soc.*, 2024, **146**, 24871–24883.

41 J. Mei, N. L. Leung, R. T. Kwok, J. W. Lam and B. Z. Tang, Aggregation-Induced Emission: Together We Shine, United We Soar, *Chem. Rev.*, 2015, **115**, 11718–11940.

42 B. Chen, W. Huang and G. Zhang, Observation of Chiral-selective room-temperature phosphorescence enhancement *via* chirality-dependent energy transfer, *Nat. Commun.*, 2023, **14**, 1514.

43 M. Molkenthin, E. Hupf and B. J. Nachtsheim, Dibenzyl isophthalates as versatile hosts in room temperature phosphorescence host–guest systems, *Chem. Sci.*, 2025, **16**, 2819–2829.

44 B. Du, Y. Wu, X. Wang, H. Tian, S. Shao and L. Wang, Multi-resonance emitters with room-temperature phosphorescence in amorphous state and excited by visible light, *Chem. Sci.*, 2024, **15**, 19432–19442.

45 J. Li, Y. Dong, R. Wei, G. Jiang, C. Yao, M. Lv, Y. Wu, S. H. Gardner, F. Zhang, M. Y. Lucero, J. Huang, H. Chen, G. Ge, J. Chan, J. Chen, H. Sun, X. Luo, X. Qian and Y. Yang, Stable, Bright, and Long-Fluorescence-Lifetime Dyes for Deep-Near-Infrared Bioimaging, *J. Am. Chem. Soc.*, 2022, **144**, 14351–14362.

46 Y. Jiang, Y. Li, F. Liu, W. Wang, W. Su, W. Liu, S. Liu, W. Zhang, J. Hou, S. Xu, Y. Yi and X. Zhu, Suppressing electron-phonon coupling in organic photovoltaics for high-efficiency power conversion, *Nat. Commun.*, 2023, **14**, 5079.

47 X. Gong, O. Voznyy, A. Jain, W. Liu, R. Sabatini, Z. Piontkowski, G. Walters, G. Bappi, S. Nokhrin, O. Bushuyev, M. Yuan, R. Comin, D. McCamant, S. O. Kelley and E. H. Sargent, Electron–phonon interaction in efficient perovskite blue emitters, *Nat. Mater.*, 2018, **17**, 550–556.

48 H. Zhang, S. Wu, Y. Liang, Z. Zhang, H. Wei, Q. Yang, P. Hu, C. Liu, Z. Yang, C. Zheng, G. Shi, Z. Chi and B. Xu, Enabling efficient and ultralong room-temperature phosphorescence from organic luminogens by locking the molecular conformation in polymer matrix, *Chem. Eng. J.*, 2024, **497**, 154949.

49 X. Zhu, Y. Jia, Y. Liu, J. Xu, H. He, S. Wang, Y. Shao, Y. Zhai and Y. Zhu, Enhancing Built-in Electric Fields *via* Molecular Symmetry Modulation in Supramolecular Photocatalysts for Highly Efficient Photocatalytic Hydrogen Evolution, *Angew. Chem., Int. Ed.*, 2024, **63**, e202405962.

50 J. V. Morris, U. Brühlmann, O. Serafimov and J. R. Huber, Excited State Behavior of Aromatic Amines in Solution: Dihydrophenazine Derivatives, *Ber. Bunsenges. Phys. Chem.*, 1974, **78**, 1348–1353.

51 L. Ma, B. Ding, Z. Yuan, X. Ma and H. Tian, Triboluminescence and Selective Hydrogen-Bond Responsiveness of Thiochromanone Derivative, *ACS Mater. Lett.*, 2021, **3**, 1300–1306.

52 L. Ma, Y. Liu, H. Tian and X. Ma, Switching Singlet Exciton to Triplet for Efficient Pure Organic Room-Temperature Phosphorescence by Rational Molecular Design, *JACS Au*, 2023, **3**, 1835–1842.

53 Q. Xu, L. Ma, S. Sun and X. Ma, Achieving visible-light-excited organic room-temperature phosphorescence by manipulating p–π conjugation, *J. Mater. Chem. C*, 2021, **9**, 14623–14627.

54 Y. Su, S. Z. F. Phua, Y. Li, X. Zhou, D. Jana, G. Liu, W. Q. Lim, W. K. Ong, C. Yang and Y. Zhao, Ultralong room temperature phosphorescence from amorphous organic materials toward confidential information encryption and decryption, *Sci. Adv.*, 2018, **4**, eaas9732.

55 M. Lv, X. Lu, Y. Jiang, M. E. Sandoval-Salinas, D. Casanova, H. Sun, Z. Sun, J. Xu, Y. Yang and J. Chen, Near-Unity Triplet Generation Promoted *via* Spiro-Conjugation, *Angew. Chem., Int. Ed.*, 2022, **61**, e202113190.